Available online at www.sciencedirect.com
SCIENCE DIRECT®
Journal of Nuclear Materials 342 (2005) 148–163
journal of nuclear materials
www.elsevier.com/locate/jnucmat

Melting of stoichiometric and hyperstoichiometric uranium dioxide

D. Manara [a], C. Ronchi [a,*], M. Sheindlin [a], M. Lewis [b], M. Brykin [c]

[a] European Commission, Joint Research Centre, Institute for Transuranium Elements, P.O. Box 2340, 76125 Karlsruhe, Germany
[b] University of Warwick, Department of Physics, Coventry CV4 7 AL, United Kingdom
[c] Joint Institute for High Temperatures, Russian Academy of Sciences, Moscow 125412, Russia

Received 25 June 2004; accepted 7 April 2005

Abstract

The solid–liquid transition in stoichiometric and hyperstoichiometric UO_2 was investigated by means of advanced techniques. Laser heating enabling fast melting and freezing processes was used under container-less conditions and buffer gas pressures up to 250 MPa, making non-congruent evaporation ineffective. Pulse thermograms of UO_{2+x} with $0 \leqslant x \leqslant 0.21$ were recorded with fast pyrometers and interpreted with computer simulations. In addition, a novel method for identification of phase transitions was implemented, based on the detection of surface reflectivity variations. The melting line of $UO_{2.00}$ was for the first time determined at pressures between 10 and 250 MPa, and the melting temperature of the stoichiometric oxide was measured to be 3147 ± 20 K, in fair agreement to previous measurements reported in the literature. The liquidus and solidus lines of UO_{2+x} differ from the currently recommended data, which substantially underrate the effect of oxygen on melting.

1. Introduction

Whilst the fusion temperature of stoichiometric $UO_{2.00}$ is well established to be in the interval $T_f = 3120 \pm 30$ K [1–9], for the non-stoichiometric oxide, $UO_{2\pm x}$, the solidus and liquidus lines are much less certain. Since at high temperatures uranium dioxide can accommodate in the fcc lattice both oxygen interstitials and vacancies over a wide stoichiometry range (at least, $1.5 \leqslant O/U \leqslant 2.25$), important variations of the melting point with stoichiometry are expected in conjunction with the appearance of an oxygen solubility gap when solid solutions $UO_{2\pm x}$ are melted. Furthermore, the melting line of $UO_{2.00}$ (i.e., the change of the melting point vs. pressure) is needed to check the relationship between thermodynamic quantities, such as density variation upon melting and related latent heat, to verify whether melting of stoichiometric UO_2 occurs congruently.

Only few experimental data were so far available [2,5,9] on melting of hyperstoichiometric UO_2, because of the difficult experimental conditions required to control and monitor the phase transition. An advanced experimental method was therefore implemented, by which most of the difficulties that negatively affected the previous measurements (high rate of non-congruent evaporation and consequent low thermochemical

* Corresponding author. Tel.: +49 7247 951 402; fax: +49 7247 951 99402.
E-mail address: ronchi@itu.fzk.de (C. Ronchi).

0022-3115/$ - see front matter © 2005 Elsevier B.V. All rights reserved.
doi:10.1016/j.jnucmat.2005.04.002

stability of the samples at high temperature) could be overcome. Pulse laser heating was adopted, whereby the temperature of the specimen was detected by a high-speed two-channel pyrometer and, in parallel, by a multichannel spectrometer. Changes induced in the sample surface reflectivity were monitored simultaneously with an additional probe laser. In order to minimise evaporation phenomena, melting was produced in an autoclave filled with inert gas at pressures up to 250 MPa.

Computer simulations were carried to support the melting-freezing thermo-analysis of the observed phenomena. Finally, a new assessment of the high-temperature UO_{2+x} phase diagram was proposed.

2. Samples

UO_2 cylindrical pellets of 8.3 mm ∅ and 12 mm height were used, fabricated by Advanced Nuclear Materials Co. Disks of approximately 4 mm thickness were cut to be fitted into the sample holder of the autoclave. They were first annealed in an alumina oven for several hours at 1273 K under an Ar + 6% H_2 flow to fix the oxygen content, determined by thermogravimetry, to O/U = 2.000 ± 0.005. The sintered density was 10.5 $g cm^{-3}$, i.e., 95% of the theoretical value.

Hyperstoichiometric samples were obtained from the original pellets after treatment in a furnace at different temperatures under an oxidising CO/CO_2 gas flow of suitable composition, according to the UO_{2+x} Ellingham diagram [10]. The resulting sample stoichiometry was first estimated by the difference in the sample weight before and after the treatment. Oxidised specimens were then subjected to the same heat treatment a second time. If upon repetition of this procedure the sample weight did not change, the parameters of the heat treatment were considered as appropriate to obtain an equilibrium composition. The exact oxygen content was then accurately measured by thermogravimetry. To make sure that the observed weight difference was due to oxidation only, some samples were reduced again to stoichiometric UO_2 in an Ar + 6% H_2 flow. The weight difference between the oxidised and the stoichiometric compounds was checked to be the same as that measured after the oxidation treatment. Chemical and morphological homogeneity was finally confirmed by optical ceramography and secondary ion mass spectroscopy (SIMS). X-ray diffraction (XRD) spectra were also analysed, confirming the phase compositions (UO_{2+x} + U_4O_{9-y}) and the lattice parameters expected at room temperature. The presence of two phases in the specimens at room temperature did not influence the melting transition measurements, as the superstructure of the oxygen interstitials of U_4O_9 rapidly disappears above ≈1400 K [11–16] transforming into UO_{2+x} solid solution.

3. Experimental

The following conditions were realised:

- Temperatures of up to 4000 K, measured with sufficient accuracy to identify phase transitions.
- No effective contamination or chemical composition changes during sample heating.
- Liquid undercooling avoided by input power control.
- Pulses fast enough to avoid convection in the buffer gas.
- Phase transition determined, regardless of possible non-equilibrium conditions in the bulk.

To satisfy these requirements an apparatus was designed and put into operation in the High-Temperature Properties Laboratory of the Institute for Transuranium Elements (ITU). The setup is sketched in Fig. 1.

3.1. High-pressure cell

The sample was held vertically in a cylindrical graphite holder fixed on a stainless steel support at the bottom of an autoclave designed for pressures up to 400 MPa. To avoid cracking of the specimen under thermal stresses, its lateral surface was wrapped in a Teflon ring. The autoclave was filled with helium since this gas causes the least optical disturbance at high pressures. Actually, pressures of the order of 100 MPa were found to be optimal in preventing evaporation from the surface without seriously perturbing pyrometric measurements. The top of the autoclave was closed by a sapphire window. A second thin window was placed inside, 1 mm above the sample surface to protect the first window from vapour convection streams – though, in general, no vapour condensation was detected on this protective window, except for slight condensation halos occasionally observed after melting of samples with O/U > 2.10.

3.2. Sample heating

The autoclave setup was placed along with the pyrometers in a safety room with reinforced explosion-proof walls and remotely operated. Two LASAG® Nd:YAG lasers were chosen with pulses programmable in length and power [8,9]. The beams (total power ≈3 kW for several tens of milliseconds) were merged in an optical mixer, channelled into the same optical fiber and simultaneously focused onto the sample surface. An energy detector was placed at the exit of the focusing optics to record the power-time profile of the pulse. The first beam supplied the main power pulse heating the sample above the melting point; the second one, separately controlled in intensity and duration, delivered a longer pulse of lower power to condition the sample cooling-rate. After random mixing inside a 15 m optical

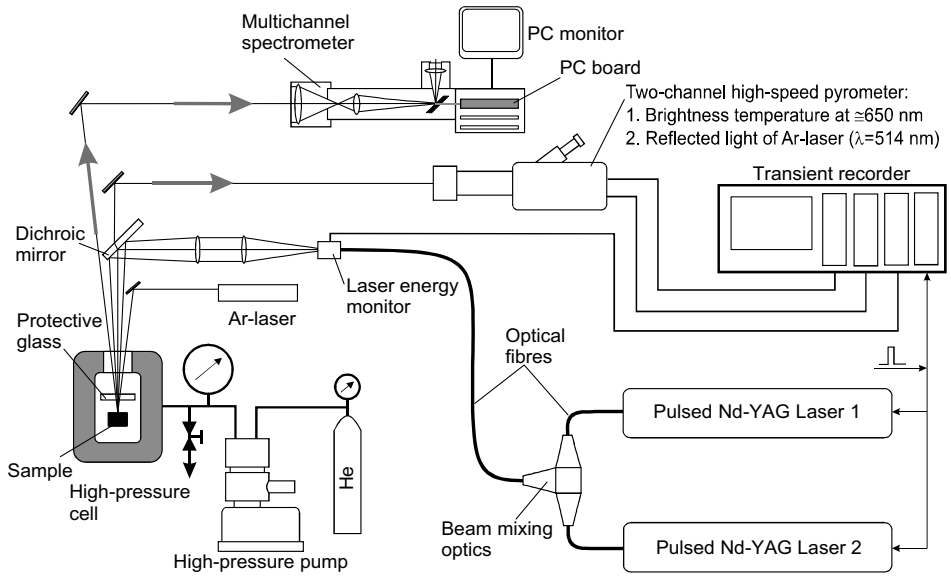

Fig. 1. Experimental equipment used in this work.

fibre a very homogeneous beam density was obtained over a focal spot of 3 mm ∅.

3.3. Measurement of the sample temperature

The surface temperature of the sample was measured by a high-speed two-channel pyrometer (1% settling time = 10 μs). Analogue signals were transferred, together with those of the energy detectors, to a Nicolet Pro 44C Transient Digitiser, externally triggered by the main switch of the two Nd:YAG laser heads. The first pyrometer channel, operating at 644 nm and calibrated against a standard band-lamp, was used for temperature measurements. The second channel was alternatively used either to provide a corroborating measurement of temperature or to detect the reflected light of a laser probe-beam to determine the instant at which melting or solidification occurred on the surface (see Section 3.5). The brightness temperature T_λ obtained at the wavelength λ was converted into true temperature by using the total transmittance of the optical path $\tau(\lambda, p_{\text{gas}})$ and the sample emissivity $\varepsilon(\lambda, T)$ in Wien's approximation:

$$\frac{1}{T} = \frac{1}{T_\lambda} + \frac{\lambda}{C_2} \ln(\varepsilon(\lambda, T) \cdot \tau(\lambda, p_{\text{gas}})), \tag{1}$$

with $C_2 = 0.0143886$ m K.

The total setup transmittance was obtained as the product of the single transmittance factors of each optical element, directly measured by means of a probe laser. A factor $\tau_{\text{gas}}(p_{\text{gas}})$ accounting for the optical effect due to the presence of high-pressure, hot gas above the sample surface was also included. Between the two sapphire windows of the autoclave (see Fig. 1) the gas was hot only in the vicinity of the sample and its density, ρ^*, between the sample surface and the first window was evaluated as

$$\rho^* = p/k_B T \ (\text{m}^{-3}), \tag{2}$$

where k_B = Boltzmann's constant and T the gas layer temperature. The optical pathway of the light beam from the sample surface was therefore:

rarefied gas/sapphire/dense gas/sapphire/air.

In order to reproduce this sequence for transmittance measurements, it was assumed that the main loss was due to reflections at the interfaces. In a simulation experiment, the spectra of the transmitted light beam were recorded by a multichannel pyrometer for different gas pressures. The spectral intensities measured at each pressure were divided by the reference values at atmospheric pressure, yielding a gas transmittance factor $\tau_{\text{gas}}(p_{\text{gas}})$ independent of the wavelength. This factor increased with increasing gas pressure due to the optical behaviour at the gas/sapphire interfaces, where the difference in refractive index between gas and sapphire decreased with increasing pressure. The total transmittance of the optical system was measured with a reproducibility of 1%.

An additional multichannel pyrometer, triggered by the transient digitiser, was focused on the sample surface. The thermal radiation emitted by the sample was detected at 256 wavelengths between 487 and 1012 nm. Spectra were recorded at successive time intervals (time resolution $\geqslant$ 0.8 ms) and fitted by a least-squares regression based on a given parametric formulation of the

emissivity-modified blackbody radiation. This analysis provided the sample temperature as well as the instantaneous spectral emissivity of the sample. The obtained values of $\varepsilon(\lambda, T)$ were only accurate enough when T-changes were slow compared with the time resolution of the multichannel pyrometer. Nonetheless, these data were always used to estimate the emissivity dependence on temperature/time. These results are near to the values of $\varepsilon(\lambda, T)$, measured by Bober et al. [17,18] and recommended by Fink [19]. No relevant effects of O/U on emissivity were detected.

3.4. Accuracy of the temperature measurements

The pyrometer setup was tested above the band-lamp calibration temperature on tungsten, obtaining a good agreement with the recommended melting point. However, none of the existing high-melting materials was suitable as a calibration standard, for the reason that their melting temperature accuracy is generally worse than that required in our experiments. Therefore, the accuracy was not directly defined in terms of standard deviations from standard values, but determined by applying the law of uncorrelated errors propagation to the temperature calibration and emissivity/transmittance uncertainties:

$$\delta T = \sqrt{\left|\frac{\partial T}{\partial T_\lambda}\delta T_\lambda\right|^2 + \left|\frac{\partial T}{\partial \varepsilon}\delta\varepsilon\right|^2 + \sum_i \left|\frac{\partial T}{\partial \tau_i}\delta\tau_i\right|^2}, \quad (3)$$

where δT_λ is the uncertainty of the temperature scale, $\delta\varepsilon$ that of the sample emissivity and $\delta\tau_i$ that of the transmittance factor in the ith optical element of the system, including the factor τ_{gas}.

Substituting the experimental values and calculating from Eq. (1) the derivatives in (3) we obtained $\delta T/T = 0.66\%$. This estimate is sufficiently conservative for measurements of the melting point of stoichiometric samples. The uncertainty affecting the melting point of hyperstoichiometric specimens was additionally affected by small changes in composition and by the difficulty in the interpretation of the solidification process thermograms. For instance, in the worst case of O/U = 2.21, the fractional dispersion of the measured transition temperature values reached ±2%.

3.5. 'Reflected light' method

A novel, very sensitive method was in addition applied to determine phase transitions, based on changes in surface reflectivity that accompany solid/liquid rapid phase transitions. A low-power argon laser ($\lambda = 514$ nm) is focused onto and reflected from the sample surface (Fig. 1). The second channel of the two-channel pyrometer is tuned on this wavelength to detect the light reflected by the sample, the intensity of which depends on the angular reflectivity. During heat-up, the first appearance of liquid on the surface causes a sudden change in reflectivity, with a sharp variation in the recorded signal. Furthermore, vibrations of the liquid mass result in oscillations of the reflected light intensity that abruptly disappear when the freezing point is reached. In this way, phase transitions can be clearly identified even in the presence of possible, complex thermal effects occurring beneath the surface.

4. Results

Fig. 2 shows the thermograms of typical melting point measurements obtained for different oxide stoichiometries. It can be immediately seen that the curves markedly change with the oxide composition, showing diverse thermal arrest features.

4.1. Stoichiometric samples

In stoichiometric $UO_{2.00}$ (thicker line in Fig. 2), a thermal arrest is visible as a plateau at the solidification temperature on the descending flank of the thermogram, whilst the power ramp is too steep for producing a detectable melting thermal arrest during heat-up. In fact, the heat delivered onto the surface per unit time is much larger that spent for melting. Only well above the melting point does a slight, reproducible decrease in slope appear, due, however, to increasing heat losses and damping of the laser power deposition.

The situation is different when the liquid mass is cooling down naturally, and equilibrium conditions are attained upon freezing: a clear thermal arrest appears, and the melting point of uranium dioxide can be determined with a precision of ±1.5 K. Experiments carried out under buffer gas pressures from 0.1 to 250 MPa

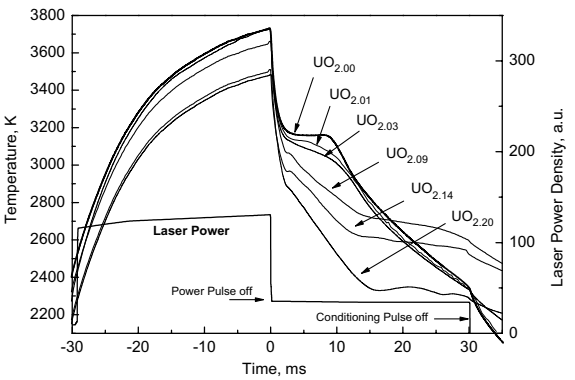

Fig. 2. Thermograms measured on stoichiometric and hyperstoichiometric uranium dioxide samples. The conditioning part of the heating laserpulse was not used in all the cases.

revealed that the freezing arrest was best defined at pressures around 100 MPa. Non-congruent evaporation from the surface was not sufficiently suppressed to reproduce this high accuracy at pressures lower than 10 MPa.

4.1.1. Melting line

The curve representing the melting point of a substance as a function of the isostatic pressure, the melting line, can be used to determine thermodynamic quantities, such as the density variation upon melting or the latent heat, or to verify if melting occurs without composition changes. In our context, the determination of the melting line of $UO_{2.00}$ constitutes an important validation of the accuracy of the experimental method.

Fig. 3 shows the freezing plateau for $UO_{2.00}$ under four different inert gas pressures. Over one hundred melting point measurements were performed in the range 10–250 MPa, with oxygen partial pressures varying from 10^{-5} to 0.05 MPa. The samples were submitted to measurements cycling over the whole pressure range with good reproducibility of the melting points.

Fitting was made on sets of results obtained at eleven different pressures. The linear regression line of the freezing point variation vs. pressure is shown in Fig. 4. The low-pressure (<50 MPa) data are slightly below the interpolated melting line, probably due to vapourisation effects leading to changes in the O/U ratio. On the other hand, at the highest pressures, optical perturbations occurred. In order to identify the influence of these different pressure-dependent effects, linear regression was performed on subsets of points covering pressure intervals of 150 MPa (0–150 MPa; 20–170 MPa; 30–180 MPa, and so on). Regression performed on pressure intervals starting from 0 up to 20 MPa, where non-congruent vapourisation was not effectively suppressed, yielded

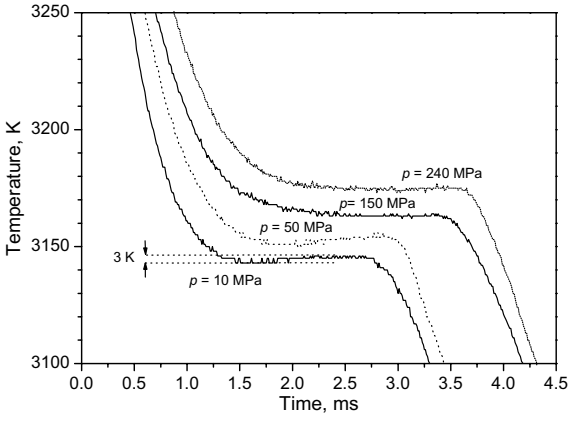

Fig. 3. Freezing stage of thermograms measured on UO_2 samples at different pressures.

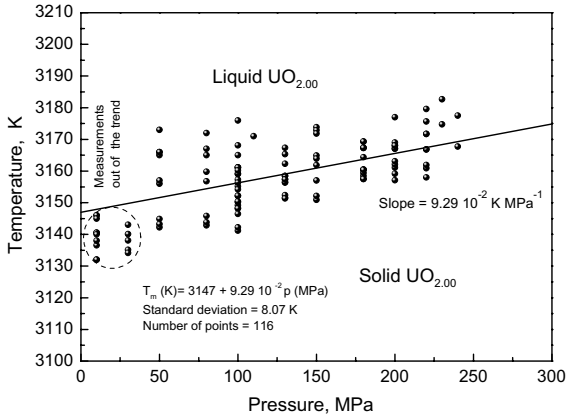

Fig. 4. Measured melting line of stoichiometric UO_2.

melting line parameters (gradient and intercept) which, being significantly different from the average of the others, were discarded. Gradients and intercepts obtained on the remaining subsets of points were averaged up. In this way, diverse effects of different experimental conditions at different pressures were averaged in the final determination of the melting line giving:

$$T_{\mathrm{m}}\ (\mathrm{K}) = 3147 + 9.29 \times 10^{-2} p\ (\mathrm{MPa}), \tag{4a}$$

where T_{m} is the melting temperature and p the isostatic gas pressure in the autoclave.

In Eq. (4a), the intercept at 3147 ± 5 K should correspond to the melting point of uranium dioxide extrapolated at zero-pressure, effectively equal to that under ambient pressure. This value is higher than that recommended of 3120 ± 30 K [1–7], although still within the uncertainty range. Yet, most melting point measurements reported in the literature were likely affected by sample contamination. Since any variation in the sample composition was ruled out in our experiments, the value obtained should be considered as the correct one for stoichiometric UO_2, with an error certainly lower than ±20 K.

The measured gradient of the melting line (melting slope, A_{m}) is

$$A_{\mathrm{m}} = (\mathrm{d}T_{\mathrm{m}}/\mathrm{d}p)_{\mathrm{exp}} = (9.29 \pm 1.70) \times 10^{-2}\ \mathrm{K\,MPa^{-1}}. \tag{4b}$$

Since this quantity is defined by the variation of the melting point, and not by its absolute value, the uncertainty of A_{m} is only due to the precision of the pyrometric measurement.

The experimental value of the melting slope can be compared to that predicted by the Clausius–Clapeyron equation:

$$\left(\frac{\mathrm{d}T_{\mathrm{m}}}{\mathrm{d}p}\right) = \frac{T_{\mathrm{m}}\Delta v_{\mathrm{m}}}{\Delta H_{\mathrm{m}}}, \tag{4c}$$

where Δv_m is the specific volume change on melting and ΔH_m the latent heat of melting. This equation describes the line of coexistence, under equilibrium conditions, of two phases having the same composition. Since the melting line is with a very good approximation a straight line, the fusion temperature at atmospheric pressure was taken for T_m with the value obtained in this work, 3147 ± 5 K. For Δv_m the value $8.26 \pm 3.3 \times 10^{-6}$ $m^3 kg^{-1}$ was calculated from the recommended density values [19,20]. For ΔH_m, the value 277.1 ± 3.7 $kJ kg^{-1}$ quoted in [21] was chosen. By substituting the chosen values in the right hand side of Eq. (4c), one obtains:

$$A_m^* = (dT_m/dp)_{calculated} = (9.38 \pm 3.75) \times 10^{-2}\ K MPa^{-1}. \quad (4d)$$

The error $\delta A_m^* = 3.75 \times 10^{-2}$ $K MPa^{-1}$ was calculated by differentiating Eq. (4c) and by applying the law of uncorrelated errors propagation:

$$\delta A_m^* = \sqrt{\left|\frac{\partial A}{\partial T_m}\delta T_m\right|^2 + \left|\frac{\partial A_m}{\partial \Delta v_m}\delta \Delta v_m\right|^2 + \left|\frac{\partial A_m}{\partial \Delta H_m}\delta \Delta H_m\right|^2}, \quad (5)$$

where δT_m, $\delta \Delta v_m$, and $\delta \Delta H_m$ indicate the uncertainties on the three parameters, representing the 66.7% confidence limits on the values reported in literature.

The agreement with the experimental average melting slope A_m is much better than expected from our conservative error analysis. This result represents an evident improvement with respect to previous experiments, where the melting point measurement was limited by less performing equipment [8], and provides a proof that the realised melting/freezing process occurred under conditions acceptably near to equilibrium. Obviously, equilibrium is only established in the molten pool, far enough from the moving solid/liquid interface. Inversely, this result can be considered as the experimental proof of the validity of the Clausius–Clapeyron equation for stoichiometric uranium dioxide, confirming that this compound melts congruently without any effective chemical change.

One can notice that the error affecting A_m^* calculated with the literature data is more than twice larger than that obtained in this work. The experimental A_m was used to deduce the value of Δv_m, the parameter affected by the largest uncertainty in Eq. (4c). We have:

$$\Delta v_m = \frac{A_m \Delta H_m}{T_m}. \quad (6a)$$

Considering the error on the experimental melting slope we obtain:

$$\Delta v_m = (8.18 \pm 1.50) \times 10^{-6}\ m^3 kg^{-1}. \quad (6b)$$

This value confirms that reported in Ref. [19], however with a smaller uncertainty.

4.2. Hyperstoichiometric samples

In order to sufficiently reduce the sample vapourisation, most of the melting point measurements on UO_{2+x} had to be performed under a gas pressure of at least 100 MPa. However, the melting point shift due to the isostatic pressure was in this case much smaller than the precision of the measurements. This was experimentally confirmed by melting $UO_{2.07}$, $UO_{2.11}$, $UO_{2.17}$ and $UO_{2.2}$ under 50, 100, 150 and 200 MPa pressure.

Typical thermograms are plotted in Fig. 2. As in the case of stoichiometric samples, no melting transition inflection is observable in the heat-up stage. As the O/U ratio slightly increases (see $UO_{2.00}$, $UO_{2.01}$ and $UO_{2.03}$ curves in Fig. 2), the thermograms show the typical features of the melting/freezing processes in a two-component system where the phase transition occurs non-congruently: the freezing arrest on the cooling flank is gradually replaced by two inflection points. The first one corresponds to the appearance of the solid phase inside the molten pool (liquidus). The cooling rate decreases at this point due to the onset of latent heat release. The second one corresponds to the temperature of total solidification (solidus). After this transition, the cooling rate increases again, indicating that liquid/solid transition is completed.

The thermograms for specimens with O/U > 2.03 are more complicated. In the cooling stage, after a first knee point (sometimes a very short thermal arrest) corresponding to the liquidus transition, a second thermal arrest occurs of unclear origin. Sometimes a slight recalescence is observed at this point (see, e.g., the $UO_{2.20}$ thermogram in Fig. 2). Such behaviour does not correspond to a regular solidus transition. Had this been the case, a second knee point should have appeared, followed by an increase of the cooling rate after complete release of the latent heat. On the other hand, the thermogram cannot be related to a monotectic transition, since in this case the temperature of the observed second thermal arrest should be the same for all compositions, whilst, as shown in Fig. 2, the lower the sample oxygen content, the higher is the temperature at which the second thermal arrest is observed.

In summary, the solidus transition could not be directly related to the second thermal arrest. However, the solidus could be determined from the 514-nm reflected light signal (RLS). Fig. 5 shows the thermogram and the RLS recorded during a melting/freezing of a $UO_{2.17}$ sample. The RLS time derivative indicates vibrations of the surface liquid layer. The RLS (dashed) curve is characterised by six different stages: (i) the signal is approximately constant as long as the sample surface is not molten; (ii) a sudden increase is observed when a very thin molten layer is formed; (iii) the amount of liquid increases to a point where the molten mass starts vibrating under capillarity forces and scattering the

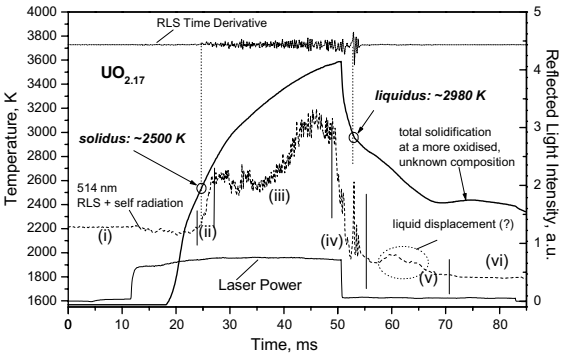

Fig. 5. Experimental thermogram recorded for a $UO_{2.17}$ sample (thick solid line). 514 nm reflected light signal and its derivative are also displayed, with the help of which six stages in the melting/freezing process could be distinguished, and solidus and liquidus transitions determined. Vertical lines across the RLS graph mark the beginning and the end of each of the six stages.

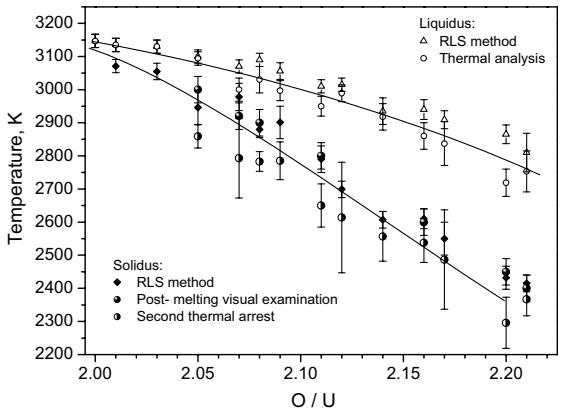

Fig. 6. UO_{2+x} solidus and liquidus points measured at several O/U compositions with the respective uncertainties. The solidus was measured by means of RLS analysis and post- melting visual examination. Post- melting visual examination of samples was performed for some compositions only. The temperatures at which the second thermal arrest was observed on the cooling stage of thermograms are also displayed. The liquidus was obtained by means of thermal arrest method and reflected light signal (RLS) analysis. The solid lines are only an eye guide.

probe laser beam (the 514 nm signal increases due to the contribution of radiation); (iv) as the first Nd:YAG laser is turned off, the solidification front advances; light scattering due to irregular motion of the liquid becomes important and is cut off when the first solid seed is formed (revealed by a spike in the RLS), a clear inflection is visible on the 644 nm channel thermogram and vibrations disappear as most of the surface freezes; (v) inhomogeneous oxygen distribution in the molten mass causes parts of the pool to solidify at different temperatures, probably leading to a radial displacement of the remaining liquid; (vi) after complete solidification, the signal stabilises at a level depending on the angular reflectivity of the recrystallised surface.

4.2.1. Measurement of the liquidus

Both thermal arrest and reflected light method were used to determine the point of first appearance of the solid phase in cooling liquid UO_{2+x} since the 'first knee point' on the thermogram cooling flank was sometimes not evident. Moreover, a considerable dispersion was found in the set of temperature measurements at which a knee point was observed. This is due to non-congruent melting/freezing occurring in the presence of fast oxygen diffusion, with consequent oxygen concentration gradients in addition to temperature gradients.

The determination of the liquidus from the thermal arrest became even more complicated if phase segregation occurred during solidification. Simulation results, presented in the next section, show that formation of oxygen concentration gradients constitutes a problem in highly oxidised (O/U > 2.10) samples. Nevertheless, the determination of the first knee point provided an evaluation of the liquidus temperature that proved to be in most cases realistic.

Since both undercooling and composition gradients depend on the duration of melting, the pulse time was reduced by nearly one order of magnitude in additional experiments. Liquidus temperatures obtained in short- and long-time experiments gave results in good agreement, ensuring that the error due to undercooling and segregation was not so large as to invalidate the measurements.

The results of the reflected light method corroborate the liquidus data obtained with the thermal arrest technique in samples with O/U < 2.15, although in general the thermal arrest provides a liquidus temperature slightly lower than that measured by the RLS method. Fig. 6 shows the liquidus points for several UO_{2+x} compositions respectively measured by thermal arrest and RLS. The difference between the two data sets increases with the oxygen content of the sample. This confirms that non-equilibrium in composition is the main cause of the discrepancy. Despite these experimental difficulties, the liquidus point could be measured within the given standard deviations in a number of UO_{2+x} samples in the range $0 < x < 0.21$.

4.2.2. Measurement of the solidus

The solidus point was determined during the heating stage with the RLS method, with a precision of approximately ±25 K. A reasonable estimate of the solidus point could also be obtained with a 'visual test', illustrated in Fig. 7(a)–(d) for samples with the same composition as that of the experiment of Fig. 5. In successive

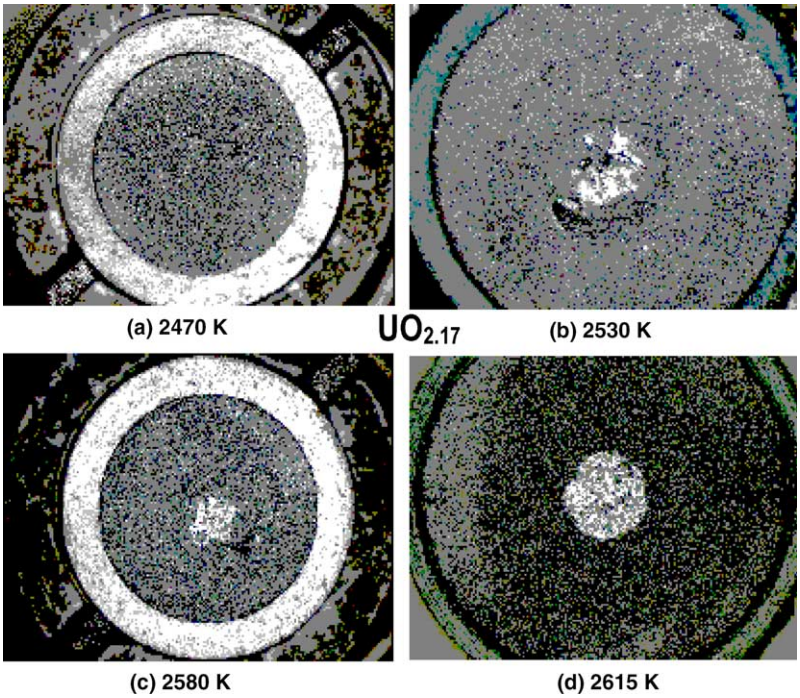

Fig. 7. (a)–(d) Post-melting visual examination to determine the solidus of a $UO_{2.17}$ specimen.

shots, the sample was pulsed at increasing temperatures and the surface was checked by optical microscopy for possible formation of liquid. The solidus point was estimated to be between 2470 and 2530 K, in good agreement with the result yielded by the RLS method. Finally, Fig. 6 displays the solidus points measured for several UO_{2+x} compositions from both RLS and post-melting observation. The agreement between the independent results proves that the deduced solidus temperatures are reliable. Fig. 6 shows, for comparison, the temperatures at which a second thermal arrest was observed on the cooling flank. Though the second thermal arrest temperatures are systematically lower than the RLS-measured solidus, the difference is mostly within the experimental uncertainty. The temperature at which the 'second thermal arrest' is observed in the highest oxidised samples ($UO_{2.20}$, $UO_{2.21}$) is a further point of interest. This temperature (approximately 2300 K) is the lowest point at which the existence of liquid UO_{2+x} has ever been observed. This can be considered as an upper bound for the temperature triple point UO_{2+x}(cr)/UO_{2+x}(l)/U_3O_{8-y}(cr) predicted by current, not fully consistent, theoretical models as in Refs. [22–24]. The data obtained in this work are summarised in Table 1. Liquidus points correspond to weighted averages of RLS and thermal arrest measurements, and solidus points from RLS and visual post-melting examination. RLS data were generally given higher statistical weights due to their better accuracy. Vertical bars correspond to the standard deviation of each experimental datum; horizontal error bars represent the uncertainty in the composition of the individual specimens.

5. Simulation and discussion of the experimental curves

5.1. One-dimensional model

A one-dimensional model was developed [25,26] to describe a two-component system heated by a laser pulse, by predicting temperature T and composition C in the sample as functions of depth z and time t, as well as the dynamics of the phase interface and the extent of the molten zone. The beam power density is assumed to be constant and cooling of the disk-shaped sample to be governed by radiative and convective heat exchange with the environment on both front and the rear surfaces ($z = 0$ and $z = L$, respectively).

The following approximations are made:

(a) The laser radiation is fully absorbed at $z = 0$.
(b) Evaporation entails heat-loss, but not mass-loss.
(c) Heat exchange inside the molten pool takes place only by thermal diffusion.
(d) On the sample rear surface heat exchange occurs through radiation only.

Table 1
Measured solidus and liquidus points in UO_{2+x}

Nominal composition/ O/U	Number of samples investigated	Pressure/GPa	Solidus/K	δT solidus/K	δx solidus	Liquidus/K	δT liquidus/K	δx liquidus
2	19	0.1	**3147**	±20	±0.005	**3147**	±20	±0.005
2.01	6	0.1	**3071**	±20	±0.005	**3135**	±20	±0.005
2.03	6	0.1	**3055**	±25	±0.005	**3130**	±20	±0.005
2.03	3	0.15	**3060**	±25	±0.005	**3115**	±25	±0.005
2.05	8	0.1	**2964**	±50	±0.005	**3098**	±20	±0.005
2.07	5	0.05	**2948**	±40	±0.005	**3028**	±40	±0.005
2.07	11	0.1	**2958**	±40	±0.005	**3070**	±20	±0.005
2.07	4	0.2	**2954**	±40	±0.005	**3063**	±40	±0.005
2.08	12	0.1	**2886**	±25	±0.01	**3075**	±20	±0.01
2.09	9	0.1	**2901**	±49	±0.005	**3056**	±25	±0.005
2.11	8	0.1	**2793**	±40	±0.005	**2995**	±20	−0.005 + 0.015[a]
2.12	9	0.1	**2699**	±25	±0.01	**3008**	±20	−0.01 + 0.02[a]
2.12	3	0.12	**2696**	±25	±0.01	**3020**	±25	−0.01 + 0.02[a]
2.14	7	0.1	**2607**	±25	±0.01	**2930**	±40	−0.01 + 0.03[a]
2.16	5	0.1	**2606**	±30	±0.01	**2920**	±30	−0.01 + 0.035[a]
2.17	3	0.05	**2528**	±50	±0.005	**2887**	±50	−0.005 + 0.04[a]
2.17	5	0.1	**2550**	±50	±0.005	**2891**	±25	−0.005 + 0.04[a]
2.17	3	0.2	**2530**	±50	±0.005	–[b]	–[b]	–[b]
2.2	12	0.1	**2438**	±35	±0.005	**2865**	±30	−0.005 + 0.055[a]
2.21	10	0.1	**2410**	±25	±0.005	**2795**	±60	−0.005 + 0.059[a]

Notes: Additional melting points measured in stoichiometric samples in the range 0.01 GPa $\leqslant p \leqslant$ 0.25 GPa are reported in Fig. 7.
[a] Uncertainty in the sample composition including the possible enrichment in oxygen, according to the simulation model.
[b] Unsuccessful measurement.

(e) The sample density ρ is constant and depends only on the state (solid or liquid).
(f) The system remains two-component throughout the experiment.

A tentative liquidus-solidus phase diagram is given as an input. The model was first validated with the better known binary system $UO_2 + ZrO_2$. In applying the simulation to UO_{2+x}, the system UO_2–O was represented as an ideal binary mixture of two uranium oxides, respectively UO_2 and $UO_{2.55}$, the latter being chosen because it is close to the eutectic composition [22,23]. The phase diagram calculated by Babelot et al. [22] in the range UO_2–$UO_{2.55}$ was taken as a first input, and was then modified by a recursive procedure, to fit the experimental results obtained in this work. According to such a phase diagram, melting can lead to violation of the oxygen homogeneity inside the sample during the melting/freezing process.

The diffusion equation describing the mass transfer within the material is

$$\rho\frac{\partial C_i}{\partial t}+\frac{\partial J_i}{\partial z}=0 \quad (i=1,2). \tag{7}$$

Here z is the depth; $\rho = \rho_1 + \rho_2$ (=const.) the total material density, and $C_i = \rho_i/\rho$, mass fraction of the component i. The quantity,

$$J_i=-\rho D\frac{\partial C_i}{\partial z} \tag{8}$$

is the diffusion flux; $D = D(C, T)$ is the temperature-dependent effective diffusion coefficient, given as an input. The caloric equation of the heat transfer in the bulk is

$$\rho\frac{\partial h}{\partial t}+\frac{\partial q}{\partial z}+\frac{\partial}{\partial z}\left(J\frac{\partial h}{\partial C}\right)=0, \tag{9}$$

where $h = h(C, T)$ is the specific enthalpy given as an input.

$$q=-\lambda\frac{\partial T}{\partial z} \tag{10}$$

is the conductive heat flux, and $\lambda = \lambda(C, T)$ is the input thermal conductivity.

The last term at the l.h.s. of Eq. (9) represents the diffusive heat transfer. The conditions connecting different values ahead of and behind the melting front (indicated by indexes $^+$ and $^-$, respectively) moving at a rate v_f, are defined by the energy and mass conservation laws:

$$J^- - J^+ = \rho v_f (C^- - C^+), \tag{11}$$

$$q^- - q^+ + \left(J\frac{\partial h}{\partial C}\right)^- - \left(J\frac{\partial h}{\partial C}\right)^+ = \rho v_f (h^- - h^+). \tag{12}$$

The above assumptions (a)–(d) define the boundary conditions for Eqs. (7) and (9). Heat transfer occurs

on the front sample surface ($z = 0$) by conduction and by evaporation. The calculation was made by using the solution of the one-dimensional non-stationary problem for a half-infinite layer, obtained by the integral heat balance method [25–27]. Input data on the gas properties were taken from [28], whereas data relative to the UO_{2+x} sample and the experimental conditions were measured for each experiment to be simulated. The input laser power was set in order to reproduce in the simulation the experimental peak temperature. Values for the diffusion coefficient $D(T, C)$ were taken for solid UO_{2+x}, from Refs. [29,30]. Enthalpy and heat conductivity were assumed to be composition-independents, and were taken from Refs. [19,31], respectively. Optical properties of the sample surface were taken from Refs. [18,19].

5.2. Discussion of the simulation results

In Fig. 8(a)–(d), an experimental thermogram measured in stoichiometric UO_2 is compared with the simulation results. Here melting occurred congruently, and no composition gradients were formed, as shown by the superficial composition curve in the figure.

Fig. 8(b) shows the simulated and empirical thermograms for $UO_{2.09}$, together with the calculated surface composition. Fig. 9 shows the concentration profile $C(z, t)$ calculated from the surface inward at eight successive times. The simulation shows that, after the onset of solidification in the bulk and on the surface, freezing occurs on two fronts, one advancing towards the surface and the other in the opposite direction. Concentration gradients are produced on both the freezing fronts, so that the very last liquid layer before total solidification was considerably enriched in oxygen. This composition heterogeneity causes an irregular release of latent heat resulting in a rather complex temperature profile, and, therefore, in the irregular shape of the thermogram around the freezing transition (Fig. 8(b)). In the real case, concentration gradients were probably less pronounced, due to the fact that diffusion occurred in three rather than one dimensions. As a consequence, the

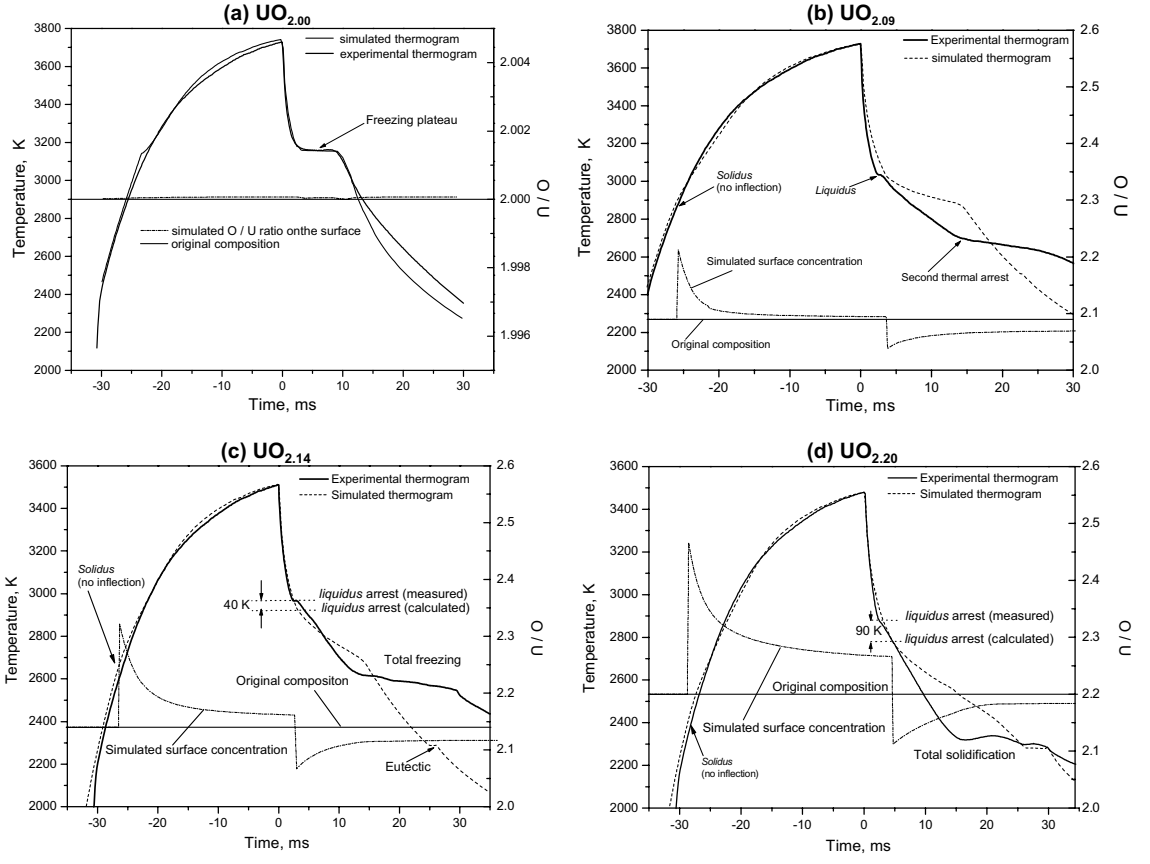

Fig. 8. (a)–(d) Experimental and simulated thermograms and simulated surface oxygen concentration trend for $UO_{2.00}$ (a), $UO_{2.09}$ (b), $UO_{2.14}$ (c) and $UO_{2.20}$ (d). According to the simulation, the large concentration gradients produced during the melting/freezing process in the most oxidised specimens – like in (c) and (d) – caused a shift of the liquidus arrest comparable with the measurement uncertainty.

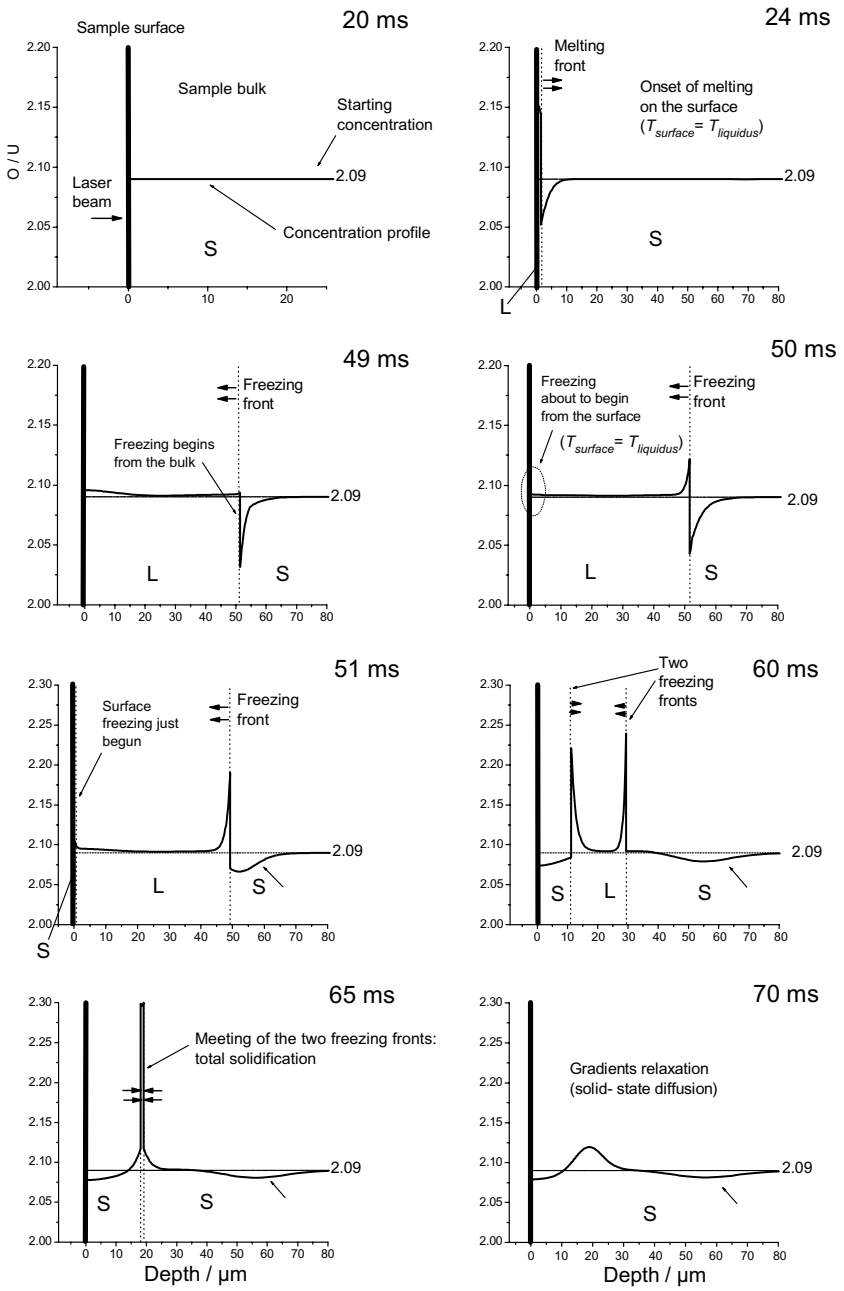

Fig. 9. Concentration profile $C(z, t)$ calculated for the melting-freezing experiment on $UO_{2.09}$ of Fig. 8(b). The sequence of graphs illustrates the effect of melting and re-freezing on the O/U ratio at different times starting from the beginning of the laser shot. The abscissa is the depth from the sample surface in micrometers. It can be seen that melting reaches the maximum penetration after 49 ms. In the following cooling phase two freezing fronts are formed travelling in opposite directions and meeting after 65 ms, leaving a residual O/U profile at the solidus point.

empirical thermogram between liquidus and solidus is smoother than that calculated. Possible deviations caused on the liquidus and solidus points by variations in the surface composition are negligible compared with the uncertainty of the measurements. The main difference with respect to the case of the stoichiometric sample consists here in the pronounced disagreement between calculated and experimental thermograms after the liquidus point is attained. By no means could the observed second thermal arrest be reproduced in the calculation.

The situation is similar in all the UO_{2+x} specimens with $0 \leqslant x \leqslant 0.10$, though the disagreement between experimental and simulated thermograms of more oxidised samples (O/U > 2.10) is more pronounced.

In the curves calculated for samples with O/U > 2.10, the position of the liquidus arrest is influenced by the variation of the oxygen distribution over the specimen during the melting-freezing process. Composition gradients in these cases are considerably higher, and, according to the one-dimensional simulation, diffusion in the liquid is not sufficient to restore the original composition on the sample surface before the onset of freezing. Fig. 8(c) and (d) shows the examples of $UO_{2.14}$ and $UO_{2.20}$ melting experiments, where the calculated oxygen content on the sample surface at the onset of freezing is still well above the starting level. In the latter example, the error in the liquidus due to the change in composition is definitely exceeding the measurement uncertainty. These results suggest that the input liquidus, based on the obtained experimental results, was somewhat inadequate for samples with O/U > 2.10.

In conclusion, the one-dimensional approximation is acceptable if thermal gradients on the sample surface are merely axial, and the growth of the crystal upon freezing is columnar, perpendicular to the surface. This was only the case for stoichiometric and moderately hyperstoichiometric samples. Fig. 10 shows SEM micrographs of $UO_{2.00}$ (a, b), and $UO_{2.08}$ (c, d) samples. Structurally, the system can be considered as one-dimensional throughout the melting-freezing process for a stoichiometric sample. With increasing stoichiometry, however, a larger 'swollen' zone in the centre of the molten surface is visible where the crystal growth is not columnar. This is probably due to movement of the liquid mass in the radial direction during the solidification process. The presence of density and concentration gradients, causing different points of the molten zone to freeze at different temperatures, was the likely origin of this effect. In this case, a one-dimensional simulation can be justified in the first part of cooling only, i.e., until the first appearance of solid in the liquid. Consequently, the typical shape exhibited by experimental thermograms after the liquidus transition could not be reproduced for compositions O/U > 2.03, irrespective of how the input parameters were changed. A corroboration of the empirical results should be sought in some experimental verification. Therefore, melting- freezing experiments of very short duration were performed on samples with O/U > 2.10. The liquidus point measured in a short pulse experiment by means of the reflected light signal analysis was in reasonable agreement with that measured in an experiment of longer duration (Fig. 11). This would not have been the case if the

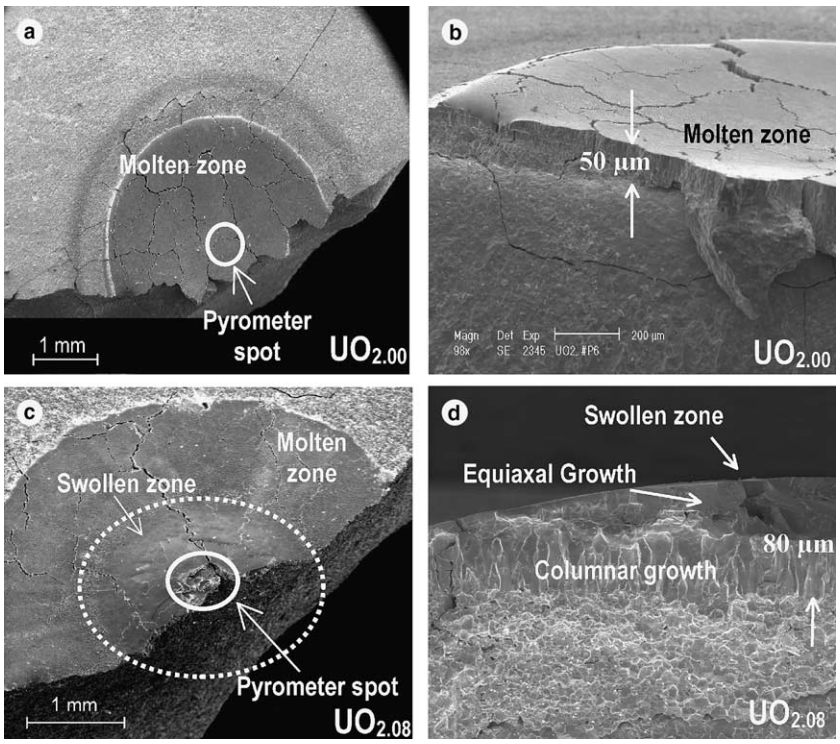

Fig. 10. SEM micrographs of samples subjected to laser induced melting/freezing experiments: (a, b) stoichiometric sample ($UO_{2.00}$); (c, d) hyperstoichiometric sample ($UO_{2.08}$).

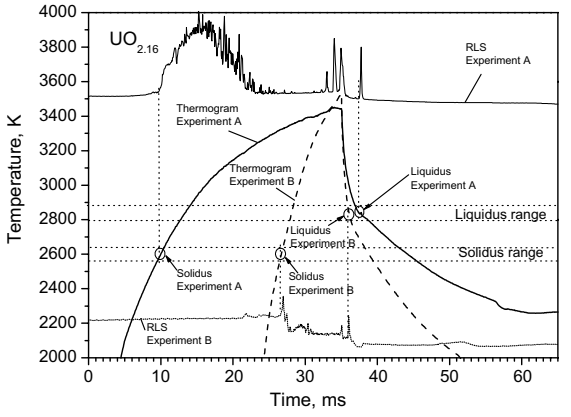

Fig. 11. Comparison between two melting point measurements performed on a $UO_{2.16}$ sample with different time regimes. In experiment A, the sample surface was kept over the melting point (solidus) for several tens of milliseconds, whereas in experiment B the existence of the liquid phase was limited to about 12 ms. Solidus and liquidus points measured by means of reflected light signal (RLS) analysis agreed in the two cases, within the uncertainty limits indicated by solid circles.

error induced by the time-dependent oxygen distribution in the liquid were decisive.

In conclusion, the one-dimensional simulation yields results in good agreement with the experimental thermograms in stoichiometric and slightly non-stoichiometric ($O/U \leqslant 2.10$) specimens, up to the first thermal inflection observed on the cooling flank of the thermograms. This confirms the reliability of the measured solidus and liquidus points.

In highly oxidised samples ($O/U > 2.10$) the effects of concentration gradients and radial liquid displacement are much more pronounced. An increased disagreement between calculated and experimental thermograms is observed, which suggests that a precautionary larger uncertainty band should be attributed to liquidus points measured in this part of the phase diagram.

6. High-temperature phase diagram of UO_{2+x}

The melting behaviour of hyperstoichiometric uranium oxide could be hardly controlled at buffer gas pressures below 10 MPa, and for the highest O/U ratios this limit had to be increased up to 100-200 MPa. These conditions might seem exceedingly rigorous for a system where the vapour pressure in the saturated thin gas layer over the liquid is in the range from 10^{-4} to 10^{-1} MPa. Yet, the largely non-congruent $UO_3(g)$ and $O_2(g)$ vapour developing over the UO_{2+x} condensed phase at a given stoichiometry may produce in the $p-T$ plane different curves defining a two-dimensional domain encompassed by the two extreme cases of (a) total equilibrium between stoichiometric liquid and non-stoichiometric vapour (boiling curve, BC), and (b) equilibrium of stoichiometric vapour with non-stoichiometric liquid (saturation curve, SC). The forced-congruent phase equilibrium (FCE) mode closer to our experiments is in-between. In the FCE mode the Gibbs energies of the condensed and vapour phases are equated by varying the pressure and imposing equal compositions. If p_v is the total vapour pressure, one can demonstrate that $p_v^{BC} \geqslant p_v^{FCE} \geqslant p_v^{SC}$ whereby at $O/U > 2.1$ the inequality may extend over orders of magnitude. A thorough discussion of this problem can be found in Ref. [32]. If one considers that under BC the O/U ratio in the vapour is more than twice that of the condensed phase, one can understand how difficult is to interpret melting experiments that just slightly deviate from the corresponding isopleths.

As mentioned at the end of Section 4, from the cooling thermal arrest observed in highly hyperstoichiometric samples, an upper bound at 2300 ± 50 K can be established for the three-phase coexistence line predicted by most UO_{2+x} thermodynamic models. Yet, the liquid phase boundary for $O/U \gg 2.1$ remains merely conjectural because at high-temperatures the vapourisation of U_3O_8 into UO_3 (g) is so fast that the melting or sublimation point could not be determined so far. In fact, by extrapolating the available thermochemical data at 2300 K, U_3O_8 should decompose in the cubic phase, UO_{2+x}, at oxygen pressures below 1.8 MPa; under these conditions the resulting equilibrium partial pressure of $UO_3(g)$ is approximately 2×10^{-2} MPa. At the highest temperature of 2700 K at which some models locate the three-phase coexistence line, the oxygen pressure threshold increases to 37 MPa with a $UO_3(g)$ partial pressure of 0.48 MPa.

Consequently, the conditions for the existence of the oxygen-rich liquid are experimentally unknown. Furthermore, from the following discussion one realises that also the theoretical models are unable to provide concordant predictions in this phase diagram area.

Table 2 shows a synopsis of available experimental and calculated data concerning the solid/liquid transition in stoichiometric and hyperstoichiometric uranium dioxide.

The only useful experimental points available prior to the present investigation were those of Latta and Fryxell [5], which are comparatively plotted in Fig. 12. Solidus and liquidus temperatures measured in [5] are generally higher than ours for compositions $O/U > 2.05$, and the disagreement becomes more pronounced at $O/U > 2.10$. This discrepancy cannot be attributed to measurement errors, but rather to an uncontrolled variation of the sample composition towards lower oxygen content in Latta and Fryxell's experiment, where the samples did likely interact with the crucible material (W or Re) with significant losses of oxygen.

Table 2
Synopsis of measurement and calculation results (T in K)

Work	Type of research	Vapour considered	$UO_{2.00}$		$UO_{2.05}$		$UO_{2.10}$		$UO_{2.15}$		$UO_{2.20}$		Three-phase coexistence line	
			Solidus	Liquidus	Solidus	Liquidus	Solidus	Liquidus	Solidus	Liquidus	Solidus	Liquidus	Temperature	Composition
This work	Exp.	Absent	3147	3147	2964	3098	2850	3025	2605	2910	2438	2865	2300	$UO_{2.23}$
Latta and Fryxell [5]	Exp.	Present	3123	3138	3000	3095	2910	3050	2900	3080	2860	3025	–	–
Babelot et al. [22]	Theor.	No	3130	3130	2975	3100	2810	3020	2698	2978	2590	2880	2420	$UO_{2.28}$
Guéneau et al. [23]	Theor.	Yes	3130	3130	2990	3095	2890	3020	2780	3000	2520	2990	2727 (slg)	$UO_{2.175}$
Chevalier et al. [24]	Theor.	No	3130	3130	3095	3110	3050	3100	2960	3065	2825	3030	2760	$UO_{2.23}$
Chevalier et al. [24]	Theor.	Yes	3130	3130	3095	3110	2900	3100	2620	3077 (*)	2340	3077 (*)	3077 (slg)	$UO_{2.067}$

Notes and abbreviations: (*) = monotectic triple line; (slg) = monotectic solid/liquid/gas line; Exp. = experimental work; Theor. = computational work.

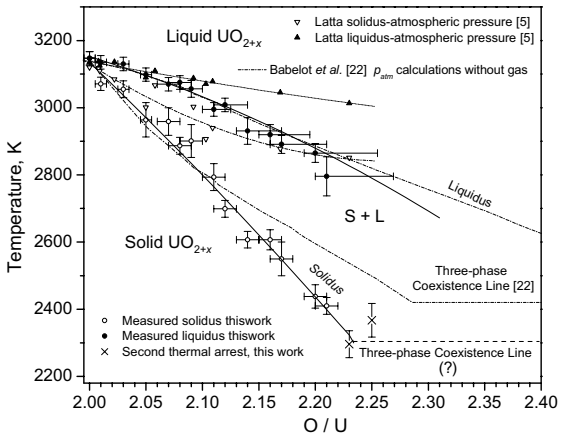

Fig. 12. Liquidus and solidus points measured in this work at 100 MPa on samples spanning several UO_{2+x} compositions, with $0 \leqslant x \leqslant 0.21$. The dotted straight lines, plotting second-order polynomial fits of the experimental points, serve as guide for the eye only. The experimental points plotted as '×' in the lower part of the graph correspond to the 'second thermal arrest' temperatures observed in the most oxidised samples, at the composition given by post-melting TG measurements on molten-refrozen zones. Latta and Fryxell data [5] and the calculated UO_{2+x} phase diagram proposed by Babelot et al. [22] are plotted too, for comparison.

Our interpolated liquidus and solidus lines are in a fairly good agreement with those calculated by Babelot et al. [22], shown in Fig. 12. The system U–O was there represented as a mixture of the three species U, UO_2 and UO_3. In particular, hypostoichiometric and hyperstoichiometric are considered as mixtures U/UO_2 and UO_2/UO_3, respectively. For these phases the interaction model of Hoch and Arpshofen [33] was used to calculate the Gibbs energy of the solid mixture and of the liquid. For compositions close to stoichiometric UO_2, the Schottky–Wagner disorder model [34] was used to calculate the concentration of U and UO_3 in UO_2. The Latta and Fryxell data [5] were employed in the analysis of the hypostoichiometric phase diagram for the optimisation of the Gibbs energy parameters describing the solubility of liquid U in solid UO_2. For UO_{2+x}, the phase boundaries were taken from the recommendations of Rand et al. [35]; free energy of mixing was calculated from existing oxygen potential measurements. UO_3 melting point and melting enthalpy were estimated by analogy with MoO_3 and WO_3. Finally, the $U–UO_3$ system was represented in [22] at atmospheric pressure, with no solid/gas and liquid/gas transitions. One can see that this model is rather simplistic and contains serious drawbacks, so that the good agreement with our results is perhaps only coincidental.

In Fig. 13 are plotted the phase boundaries calculated by Guéneau et al. [23]. In their model, solid urania is considered as an ionic triple-sub lattice structure, the

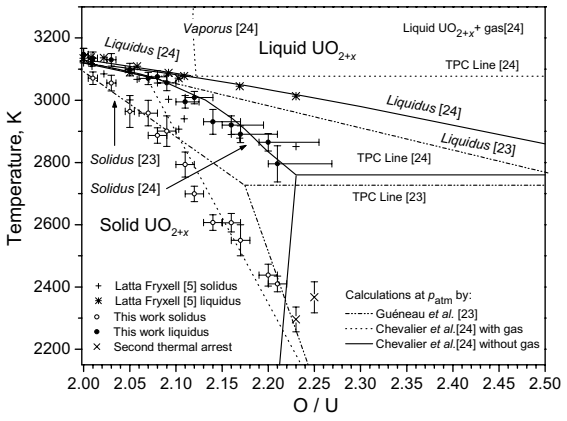

Fig. 13. Comparison between urania solidus and liquidus lines measured in the present work at 100 MPa and the same phase boundaries calculated by Guéneau et al. [23] and by Chevalier et al. [24] at atmospheric pressure.

liquid phase is treated as an ionic double-sub lattice (anionic and cationic) compound. The liquidus and solidus lines of Latta and Fryxell were used, corrected according to Raoult's cryoscopy law to take into account the dissolution of tungsten in the liquid during the melting experiments. Gibbs energy calculations were performed in [23] at atmospheric pressure taking into account the liquid/gas and solid/gas phase transitions. A three-phase coexistence line $UO_{2.17}$(s)/$UO_{2.55}$(l)/UO_3(g) was obtained at 2727 K, a value that cannot be compared with the results obtained in this work. On the other hand, the phase boundaries calculated in [23] and the results of the present work are in a sufficient agreement for O/U < 2.1.

In the calculations performed by Chevalier et al. [24] (see Fig. 13), $UO_{2\pm x}$ was represented by a 'three-sublattices' model, similar to the one used by Guéneau et al. The liquid was supposed to be a mixture of pure species $U_{(L)}$ and $O_{(L)}$ and associated species, $UO_{2(L)}$. Under this assumption, the stoichiometry field was described by the interaction parameter between $O_{(L)}$ and $UO_{2(L)}$ in the liquid in correlation with the UO_{2+x} solid-solution model. The phase diagram at atmospheric pressure was calculated both with and without the gas phase, the latter condition being closer to our experiments. A three-phase coexistence line $UO_{2.25}$(s)/U_3O_8(s)/UO_3(l) was obtained at approximately 2750 K (though the exact co-ordinates of invariant points of this transformation are not very clear in Ref. [24]). If the condensed phase/gas transitions were taken into consideration, a transition $UO_{2.07}$(s)/$UO_{2.12}$(l)/UO_3(g) was obtained at 3077 K. In describing the solid–liquid transition, Gibbs energy parameters were calibrated from the Latta and Fryxell data. As a consequence, liquidus and solidus lines proposed in [24] fit these experimental points in the range $UO_{2.00}$–$UO_{2.25}$, and are consequently in disagreement with the phase boundaries found in our work.

In conclusion, one can see that an effort is still necessary to ameliorate the thermodynamic models of UO_{2+x} by starting from the new experimental data and self-consistent assumptions. Further experimental and theoretical work is in progress at ITU on this subject [36].

7. Summary and conclusions

New experimental evidence on the melting behaviour of stoichiometric and hyperstoichiometric uranium dioxide was obtained:

- The melting line of UO_2 was for the first time measured in the range 10–250 MPa, confirming congruent melting of the stoichiometric dioxide.
- In the composition range $UO_{2.00}$–$UO_{2.21}$ melting was produced and analysed under a buffer gas pressure of 100 MPa, under conditions where the solidus and liquidus lines could be accurately measured. The effect of excess oxygen on the decrease of the melting point of the cubic structure is much more pronounced than previously assumed.
- From the measured data a high-temperature phase diagram of UO_{2+x} was obtained, at pressures up to near the triple point at each composition investigated. On the other hand, the onset of massive evaporation, observed at atmospheric pressure and at temperatures close to the melting point, indicates that realistic theoretical descriptions of the UO_{2+x} system at atmospheric pressure must take into account the formation of vapour from the condensed phase.
- High temperature UO_2–O phase diagrams as calculated from existing theoretical models are generally in poor agreement with the experimental results of this work. This incongruity clearly stems from the marked difference between our results and those of Latta and Fryxell [5], which have been generally used until now to calibrate the models. Therefore, the new results suggest that a revision of the current views on the UO_{2+x} system is necessary.

Acknowledgement

This work was carried out within the 6th Framework Programme of the European Commission as a part of the action 'Safety of Nuclear Fuel'.

References

[1] J.L. Bates, J. Am. Ceram. Soc. 49 (1966) 395.

[2] J.A. Christensen, Stoichiometry Effects in Oxide Nuclear Fuels, Battelle Northwest (USA), Laboratory Report 536, 1967.
[3] W.L. Lyon, W.E. Baily, J. Nucl. Mater. 22 (1967) 332.
[4] M.J. Bannister, J. Nucl. Mater. 24 (1967) 340.
[5] R.E. Latta, R.E. Fryxell, J. Nucl. Mater. 35 (1970) 195.
[6] T. Tachibana, T. Ohmori, S. Yamananouchi, T. Itaki, J. Nucl. Sci. Technol. 22-2 (1985) 155.
[7] S. Yamanouchi, T. Tachibana, K. Tsukui, M. Oguma, J. Nucl. Sci. Technol. 25-6 (1988) 528.
[8] D. Manara, C. Ronchi, M. Sheindlin, Int. J. Thermophys. 23 (2002) 1171.
[9] D. Manara, C. Ronchi, M. Sheindlin, High Temp. High Press. 35/36 (2003/2004) 25.
[10] B. Lindemer, T. Besman, J. Nucl. Mater. 130 (1985) 473.
[11] B.E. Schaner, J. Nucl. Mater. 2 (1960) 110.
[12] A. Saito, J. Nucl. Mater. 51 (1974) 112.
[13] A. Nakamura, T. Fujimo, J. Nucl. Mater. 149 (1987) 80.
[14] S. Aronson, J.E. Rulli, B.E. Schaner, J. Chem. Phys. 35 (1961) 24.
[15] W. Van Lierde, J. Pelsmaekers, A. Lecocq-Robert, J. Nucl. Mater. 37 (1973) 276.
[16] L.E.J. Roberts, A.J. Walter, J. Inorg. Nucl. Chem. 22 (1961) 213.
[17] M. Bober, J. Singer, K. Wagner, J. Nucl. Mater. 124 (1984) 120.
[18] M. Bober, H.U. Karow, K. Müller, High Temp. High Press 12 (1980) 161.
[19] J.K. Fink, J. Nucl. Mater. 279 (2000) 1.
[20] W.D. Drotning, in: Proceedings of the 8th Symposium on Thermophysical Properties, Gaithersburg, MD, 15–18 June 1981, Nat. Bur. Stand., 1981.
[21] J.H. Harding, D.J. Martin, P.E. Potter, Thermophysical and Thermochemical Properties of Fast Reactor Materials, Harwell Laboratory UKAEA Report EUR 12402, 1989.
[22] J.F. Babelot, R.W. Ohse, M. Hoch, J. Nucl. Mater. 137 (1986) 144.
[23] C. Guéneau, M. Baichi, D. Labroche, C. Chatillon, B. Sundman, J. Nucl. Mater. 304 (2002) 161.
[24] P.-Y. Chevalier, E. Fischer, B. Cheynet, J. Nucl. Mater. 303 (2002) 1.
[25] V.V Atrazhev, M.V. Brykin, 'Numerical Simulation of Melting and Solidification of Binary Mixtures in Laser Heating Pulses (Non-Congruent Phase Transition Solid-Liquid)', Report 17644-2001-03F1SC KAR RU, European Commission, JRC-ITU, Karlsruhe, Germany.
[26] D. Manara, M. Sheindlin, M. Lewis, Int. J. Thermophys. 25 (2004) 533.
[27] M.V. Brykin, V.S. Vorobiev, B.V. Sheluchaev, Tepl. Vys. Temp. 25 (1987) 2 (in Russian).
[28] Gmelin, Handbook of Inorganic Chemistry, Helium, 8.Aufl. XXXII, VII, Springer Verlag, Berlin, 1926.
[29] W. Breitung, J. Nucl. Mater. 74 (1978) 10.
[30] P. Ruello, G. Chirlesan, G. Petot-Ervas, C. Petot, L. Desgranges, J. Nucl. Mater. 325 (2004) 202.
[31] Ronchi, M. Sheindlin, M. Musella, G.J. Hyland, J. Appl. Phys. 85 (1999) 776.
[32] C. Ronchi, I. Iosilevski, E. Yakub, Equation of State of Uranium Dioxide (Chapter 4), Springer Verlag, Berlin, Heidelberg, New York, 2004.
[33] M. Hoch, I. Arpshofen, Z. Metallk. 75 (1984) 23.
[34] C. Wagner, W. Schottky, Z. Phys. Chem. B 11 (1931) 163.
[35] M.H. Rand, R.J. Ackermann, F. Groenvold, F.L. Oetting, A. Pattoret, Rev. Int. Hautes Tempér. Réfract. Fr. 15 (1978) 355.
[36] E. Yakub, I. Iosilevski, C. Ronchi, Defect interaction and order–disorder transitions in non-stoichiometric ionic solids, in: 11th International Workshop on the Physics of Non-ideal Plasmas, Valencia, Spain, March 21–25, 2003.